nature astronomy

ARTICLES

https://doi.org/10.1038/s41550-019-0933-6

A measurement of water vapour amid a largely quiescent environment on Europa

L. Paganini[1,2*], G. L. Villanueva[1], L. Roth[3], A. M. Mandell[1], T. A. Hurford[1], K. D. Retherford[4] and M. J. Mumma[1]

Previous investigations proved the existence of local density enhancements in Europa's atmosphere, advancing the idea of a possible origination from water plumes. These measurement strategies, however, were sensitive either to total absorption or atomic emissions, which limited the ability to assess the water content. Here we present direct searches for water vapour on Europa spanning dates from February 2016 to May 2017 with the Keck Observatory. Our global survey at infrared wavelengths resulted in non-detections on 16 out of 17 dates, with upper limits below the water abundances inferred from previous estimates. On one date (26 April 2016) we measured 2,095 ± 658 tonnes of water vapour at Europa's leading hemisphere. We suggest that the outgassing of water vapour on Europa occurs at lower levels than previously estimated, with only rare localized events of stronger activity.

Galileo observations showed that Europa's mottled landscape consists of chaotic terrains with pits, domes, platforms, irregular uplifts and lobate features[1,2]. Analysis of these features, along with radio doppler data, suggested that Europa contains a layer of water, a silicate mantle and a metallic core[3–6]. The water layer, presumed to be a thin ice sheet (~5–20 km thick) covering a putative global ocean (~60–160 km deep), has strong implications for the discovery of biosignatures beyond Earth, where the buoyant icy shell would insulate the underlying ocean, potentially allowing it to survive a hostile surrounding environment for geological timescales, and precluding penetration of harmful radiation below depths of ~1 m (ref. [7]).

Over the past few decades, theoretical modelling and remote observations have revealed diverse dynamic processes that modify Europa's icy surface and shape its atmosphere. Jovian plasma, solar radiation and meteoritic impacts influence the Europan environment not only by modifying the surface composition (for example, through radiolysis) but also by populating Europa's tenuous atmosphere, where strong energetic radiation and thermal desorption feed the atmosphere with particles stripped from its surface. These exogenic processes yield substantial quantities of water, along with atomic/molecular oxygen and hydrogen, and alkali metals[8–11]. Theoretical models[12,13] estimate that exogenic sources of the most abundant surface species (H_2O, O_2 and H_2) populate the atmosphere at rates of ~10^{26}–10^{27} molecules s^{-1}. Plumes, on the other hand, act as endogenic mechanisms[14]—probably driven by tidal flexing—that sporadically feed Europa's atmosphere with particles from the global ocean, or intermediate liquid pockets, at rates (>10^{28} molecules s^{-1}) that can surpass those from exogenic effects.

Estimates of water vapour on Europa (either from exogenic or endogenic sources) have relied strongly on modelling efforts, yet confirmation from observational data has been lacking. In 2012, ultraviolet observations[15] with the Hubble Space Telescope (HST) found simultaneous auroral emission features of hydrogen and oxygen in the southern hemisphere, at abundances greater than 10^{29} molecules s^{-1}, which exceeds the values expected from exogenic effects by factors of 100–1000. This was the first successful detection and characterization of plume content on Europa. These spectroscopic measurements of plume-like H and O emissions, however, have not yet been confirmed despite numerous attempts, making detection of these features an elusive endeavour. Recent transit imaging[16] and reanalysis of Galileo magnetic and plasma field data have served as independent assessments of plume activity[17,18]. However, the intrinsic characteristics of these observations preclude direct determination of water.

In 2016, we began an observing programme aimed at characterizing the chemical composition of Europa's atmosphere—particularly water vapour—with the near-infrared spectrograph (NIRSPEC) at the 10-m Keck Observatory. The key advantage of observations at infrared wavelengths is the ability to measure H_2O (not H and O), thereby providing a direct and independent assessment of water vapour in Europa's atmosphere (see Supplementary Fig. 1). In the nearly collisionless environment, solar excitation of molecules (water and organics) results in the emission of infrared photons through decay to the ground vibrational state, either directly (resonant fluorescence) or through branching into intermediate vibrational levels (non-resonant fluorescence), allowing these signatures to be detected using high-resolution spectroscopy. We targeted radiative excitation of water molecules via solar excitation in the 2–5.5-μm wavelength range, along with organics such as ethane, methanol, methane, hydrogen cyanide, formaldehyde and ammonia (depending on the instrument configuration). Our survey consisted of 17 observations, spanning dates from February 2016 to May 2017 (see Tables 1 and 2 for details). Multiple visits were needed to provide full longitudinal sampling and temporal coverage to probe the possible cadence of water vapour activity, and included some back-to-back observations of particular regions after a single orbital period (3.55 d). We obtained disk-averaged measurements of Europa, as defined by the instrument slit of 0.4″ width (or 0.7″, depending on the night's 'seeing') and spatial extract of ~1″ along the north–south or east–west direction.

Of the 17 observations, our results on 16 dates indicated no detection of atmospheric emission features within sensitivity limits, thus establishing a rather quiescent state. The sensitive upper limits for water outgassing indicated column densities as low as

[1]NASA Goddard Space Flight Center, Greenbelt, MD, USA. [2]American University, Washington, DC, USA. [3]KTH Royal Institute of Technology, Stockholm, Sweden. [4]Southwest Research Institute, San Antonio, TX, USA. *e-mail: lucas.paganini@nasa.gov

Table 1 | Atmospheric conditions during observations

Observation date and time (UT)[a]	RH[b] (%)	Wind[b] (mph)	Mean seeing (DIMM)[b]	Airmass[c]	PWV1[c] (mm)	PWV2[d] (mm)
3 February 2016 11:31	20	10	0.96	1.1	1.2	0.9–1.1
3 February 2016 13:14	21	0	0.96	1.1	1.0	0.9–1.1
5 February 2016 13:48	4	1	0.60	1.2	0.6	0.6–0.7
10 February 2016 11:55	18	22	0.78	1.1	0.7	1.1–1.5
12 February 2016 11:09	11	20	0.51	1.0	0.7	0.6–0.8
12 February 2016 14:17	12	15	0.51	1.4	0.6	0.6–0.8
19 February 2016 10:52	12	0	0.51	1.0	0.6	0.7–0.9
27 February 2016 11:06	5	14	0.51	1.1	0.8	0.7–0.9
12 April 2016 06:29	14	15	0.74	1.0	0.7	0.8–1.0
19 April 2016 07:46	16	3	0.55	1.1	1.2	0.9–1.1
26 April 2016 05:32	9	0	0.52	1.0	0.8	0.7–0.9
29 April 2016 08:10	6	13	0.72	1.1	1.5	1.0–1.5
11 February 2017 11:48	18	50	n/a	1.2	4.8	3.5–4.5
17 February 2017 10:47	13	11	0.49	1.5	1.4	1.0–1.2
05 March 2017 11:10	11	20	0.52	1.1	3.4	3.5–4.5
12 March 2017 10:22	30	0	n/a	1.1	3.7	4.0–6.0
15 March 2017 7:50[a]	26	0	0.69	1.7	2.8	3.0–4.0
19 March 2017 11:47	35	24	0.77	1.1	3.8	2.5–3.5
22 March 2017 13:29	8	6	0.59	1.4	1.6	1.8–2.2
07 May 2017 13:29	18	0	0.71	1.2	2.0	1.3–1.8

[a]These values represent the midpoint of data acquisition. [b]Relative humidity (RH), wind and mean seeing obtained from Maunakea Weather Center (MKWC) (http://mkwc.ifa.hawaii.edu/current/seeing/index.cgi). [c]Airmass and precipitable water vapour (PWV1) obtained from our retrieval algorithm. [d]Predicted precipitable water vapour (PWV2) obtained from MKWC's archive forecast data (http://mkwc.ifa.hawaii.edu/forecast/mko/archive/index.cgi).

1.3×10^{19} H_2O m^{-2} and 2.6×10^{19} H_2O m^{-2} (3σ) in 2016 and 2017, respectively. One measurement, however, yielded an indication of spectral emission suggesting the presence of water vapour on 26 April 2016 (Fig. 1), at sub-observer longitude of ~140° ± 40° (leading hemisphere), when Europa was near apocentre (true anomaly ~159–176°). The signal-to-noise ratio (SNR) of the retrieved H_2O spectrum (3.1σ) prevents us from establishing a definitive detection, yet co-addition of several spectral water lines and cross-correlation analysis of the observed spectra provide further statistical significance, corroborating the presumed water activity. Details of the data analysis and statistical approaches can be found in the 'Data analysis' section of the Methods. In Fig. 1, we show results from observations on similar longitudes during orbits that were contemporary with the detection date, before (12 and 19 April) and after (29 April), suggesting that the presence of water vapour on 26 April 2016 was an isolated event. Supplementary Figs. 2, 3, 7 and 8 show the results from the entire observing campaign during 2016 and 2017. The measurement of water output on 26 April 2016 corresponds to a mean column density of $(1.4\pm0.4)\times10^{19}$ H_2O m^{-2}, totalling $(7.0\pm2.2)\times10^{31}$ molecules in the field of view subtended by our observations on that date (~1,491 × 3,420 km^2).

With regard to other volatiles, we did not detect methanol nor ethane at upper limits (3σ) of 1.9×10^{18} CH_3OH m^{-2} and 3.0×10^{17} C_2H_6 m^{-2} (that is, mixing ratios of <14.3% CH_3OH and <2.2% C_2H_6 relative to water on 26 April 2016). Although not restrictive, these upper limits provide context to expected column densities resulting from plumes and/or sputtering (10^{13}–10^{16} CH_3OH m^{-2} and 10^{14}–10^{18} C_2H_6 m^{-2}, based on theoretical models[19]). The chosen instrument configuration precluded us from obtaining measurements of other trace species (mainly, HCN, CH_4, NH_3 and H_2CO) on 26 April 2016.

Is the observed water vapour a consequence of endogenic (plume-driven) activity or exogenic effects (sputtering, sublimation, impacts)? We favour the first interpretation. Theoretical models provide differing results regarding the predicted water yields from exogenic processes, with some studies estimating water column densities of ~10^{16} H_2O m^{-2} (refs. [11,13,20]), while others predict ~10^{18}–10^{19} H_2O m^{-2} (refs. [19,21]). Using this information—and noting the dissimilar predictions—we identify opposing views to the possible origin of the observed water vapour: (1) an interpretation that suggests our water measurement (of ~1.4×10^{19} H_2O m^{-2}) surpasses the mass volume expected from exogenic sources by at least three orders of magnitude (implying an endogenic source) versus (2) the contrasting view that the detected water levels could result from exogenic effects. Most of these models indicate that the higher yields are expected on Europa's trailing hemisphere[12], yet our measurement of water vapour occurred during observations of the leading hemisphere (see sub-observer longitudes in Table 2). Moreover, most of our observations resulted in non-detections at upper limits of ~10^{19} H_2O m^{-2}, both on the trailing and leading hemispheres (Fig. 2), so if one assumes that exogenic sources produce water vapour at somewhat constant rates, we should have measured water vapour more than once. Similarly, if one considers the expected production rates using a simple plume model, we estimate a total water production rate of $(7.9\pm2.5)\times10^{28}$ molecules s^{-1} (~ 2,360 ± 748 kg s^{-1}; see the subsection 'Calculation of column density and production rates' in Methods), which is at least a factor of ten larger than global values expected from sputtering and desorption of the icy water surface[12] of ~10^{26}–10^{27} molecules s^{-1}. Therefore, considering that our ground-based observations are sensitive to somewhat large amounts of water vapour rates (~10^{28} molecules s^{-1}), the 26 April data suggest that the water vapour measured in 2016 resulted from a singular, localized event that increased the water abundance to detectable limits (of a few 10^{19} H_2O m^{-2}), as would be the case of endogenic activity[19].

Table 2 | Results from our infrared observations including the 16 non-detections (upper limits, 3σ) and the water detection on 26 April 2016

Observation date and time (UT)[a]	Time on source (min)	Spatial resolution (km² per pixel)	Spectral extract (pixels)	Slit	Sub-observer longitude (° W)	TA (°)	Europa diameter (″)	Total water molecules ($\times 10^{32}$)[b]	Total water molecules ($\sigma \times 10^{32}$)
3 February 2016 11:31	61	662×482	15	NS	17–24	347–354	0.9	<2.05	0.68
3 February 2016 13:14	97	662×481	15	EW	24–35	354–5	0.9	<1.60	0.53
5 February 2016 13:48	100	658×479	15	NS	230–240	201–204	0.9	<0.93	0.31
10 February 2016 11:55	164	653×475	15	NS	9–26	344–1	0.9	<1.14	0.38
12 February 2016 11:09	124	650×473	25	NS	209–222	184–198	1.0	<1.12	0.37
12 February 2016 14:17	64	650×473	25	EW	222–229	198–205	1.0	<1.09	0.36
19 February 2016 10:52	152	643×468	15	NS	198–215	178–196	1.0	<0.62	0.21
27 February 2016 11:06	132	639×465	15	NS	291–306	277–292	1.0	<0.58	0.19[c]
12 April 2016 06:29	105	661×481	15	NS	158–171	174–188	0.9	<0.76	0.25
19 April 2016 07:46	60	672×489	15	NS	154–160	174–181	0.9	<1.07	0.36
26 April 2016 05:32	148	684×497	15	NS	134–150	159–176	0.9	0.70	0.22
29 April 2016 08:10	24	690×502	15	NS	90–94	115–120	0.8	<1.50	0.50
11 February 2017 11:48	88	690×502	15	NS	257–268	19–28	0.9	<1.50	0.50
17 February 2017 10:47	32	692×503	15	NS	346–359	268–272	0.9	<2.30	0.77
5 March 2017 11:10	70	664×483	15	NS	170–175 186–191	100–105 117–120	0.9	<1.64	0.55
12 March 2017 10:22	161	655×476	15	NS	157–174	92–109	0.9	<1.22	0.41
15 March 2017 07:50[a]	46	652×474	15	NS	91–100	30–39	0.9	<6.99	2.33[d]
19 March 2017 11:47	52	648×471	15	NS	154–159	93–98	1.0	<1.88	0.63
22 March 2017 13:29	55	646×469	15	NS	105–110	48–54	1.0	<2.18	0.73
7 May 2017 13:29	92	657×477	15	NS	61–70	32–42	0.9	<1.21	0.40

[a]All observations were taken using a KL filter (~2.9 μm), except 15 March 2017, which used an M-band filter (~5.5 μm). NS, north–south; EW, east–west; TA, true anomaly. [b]Assumed rotational temperature: 50 K. Column density is N_{col} (molecules m^{-2}) = total water/(spatial resolution × spectral extract × 10^6). [c]Most sensitive observation. [d]Least sensitive observation.

Once in the atmosphere, the fate of the released water molecules will depend on the solar radiation, the Jovian plasma field and Europa's gravitational field, leading to one (or more) of the following mechanisms: excitation, ionization, dissociation, return (freeze out) and/or escape. Most water molecules will return to the surface and freeze out, due to Europa's large escape velocity of 2,000 m s^{-1} and a high sticking coefficient. It is estimated that ~42–86% of the material ejected from all exogenic and endogenic sources returns to the surface, with models[22] showing a total erosion rate of ~0.0147 μm yr^{-1}. A small fraction of the plume water will be dissociated into OH, H, O and/or H_2. Electron impact dissociation, likely to be the dominant dissociative mechanism[23], will dissociate ~1% of water or less[24]. This estimate assumes a residence time of water molecules in the atmosphere of hundreds of seconds (~887 s, as defined by ballistic trajectories: $t \approx 2v/g$, where v is the mean molecular speed of ~ 583 m s^{-1} at 273 K, and g is Europa's gravity of 1.315 m s^{-2}), and an electron impact dissociation rate[23] on the order of ~10^{-5} s^{-1}. HST was able to detect such a small (electron-excited) population of H and O in December 2012[15].

To put our global observations in context, we compare our most sensitive H_2O data at different Europan longitudes with HST indirect estimates of water in 2012[15] and 2014[16] (see Fig. 2). We stress that these measurements sampled different physical mechanisms, given that previous techniques with HST were sensitive either to total absorption or atomic emissions. With that in mind, the HST measurements of auroral emission[15] estimated a total water content of $(13 \pm 3) \times 10^{31}$ molecules near ~180° W, while the transit observations[16] led to estimates on three different dates near ~270° W, with values ranging $(4–25) \times 10^{31}$ molecules and a median value of 18×10^{31} molecules. Our infrared observations indicate upper limits for water vapour of ~6×10^{31} at similar longitudes (that is, a factor of 2–3 lower amount of water vapour on the trailing hemisphere, using data on 19 and 27 February 2016). Even though the positions of active areas differ significantly—especially with the transit observations (~270° W longitude)—and the time of acquisition was different, the HST rates of water release agree with Keck measurements ($(7.0 \pm 2.2) \times 10^{31}$ H_2O molecules) within 2σ uncertainties.

Observations at different orbital positions with respect to Jupiter (true anomaly) allowed the study of tidal effects on the presumed activity (see Supplementary Fig. 11). The H_2O detection on 26 April 2016 by Keck and the 2012 H and O detection by HST[15] occurred near Europa's apocentre (contrary to the HST transit observations[16]; see Supplementary Fig. 4). Plume activity may be expected at certain orbital locations if tidal cycles force active geology, and this hypothesis has been foundational when attempting predictions of locus and variation in plume activity. For instance, on Enceladus, eruptions of plume material have been linked to tidal stresses[25], and observations from Cassini's Visible and Infrared Mapping Spectrometer (VIMS) verified that tidal activity varies on an orbital timescale[26], with maxima near the apocentre. As mentioned already, our infrared survey of Europa provided uniform measurements at different orbital positions, yielding temporal coverage appropriate to constrain the activation of plumes driven by tidal effects, yet results suggest no direct evidence of repeated activity within sensitivity limits in our survey. The latter is in line with theoretical analysis[27] of hypothetical active fractures under tidal stress that suggested no correlation between large-scale plume activity and source location; this indicates that the presence of active, large fractures is unlikely on Europa, in contrast to Enceladus's 'tiger stripes'. Moreover, analysis of possible source regions was hampered by the existing surface resolution

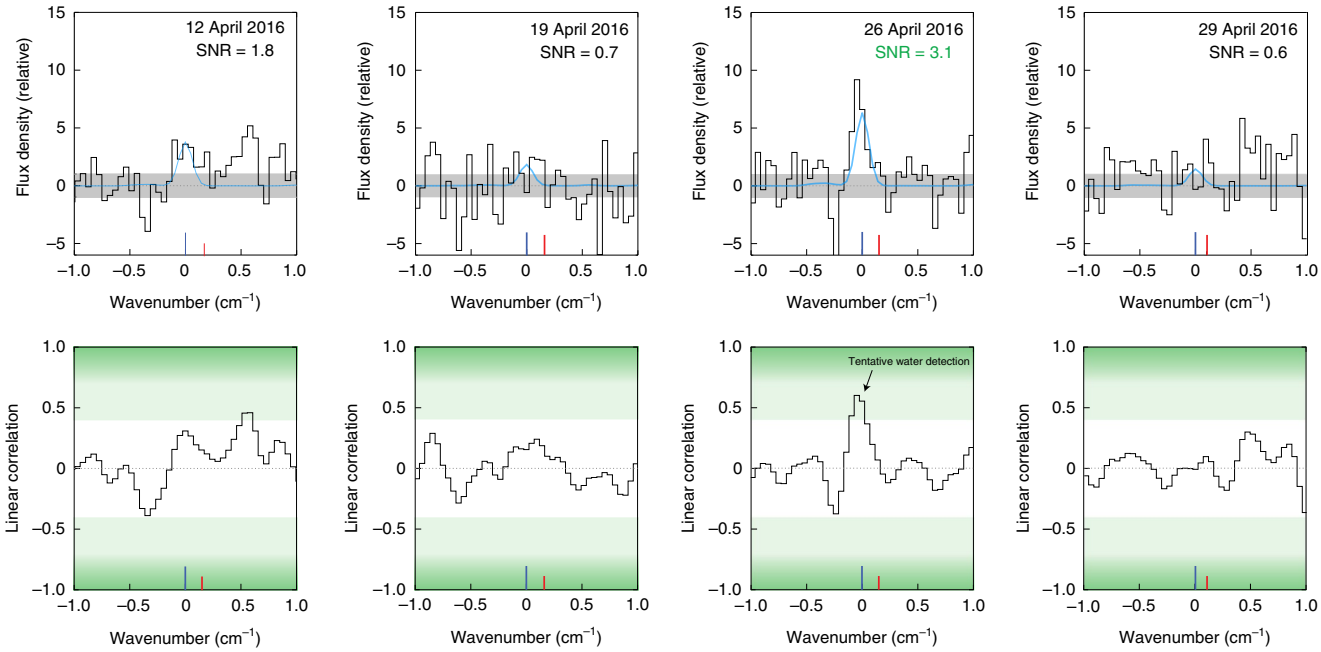

Fig. 1 | Spectra of co-added water lines in April 2016. Observations of similar longitudes during orbits that were contemporary with the detection date, before (12 and 19 April) and after (29 April), suggest that the presence of water vapour on 26 April 2016 was an isolated event. Top: the light blue line shows the co-added fluorescence model of the seven most significant water lines, the dark blue and red lines indicate the expected position of Europan and terrestrial water, and the grey shaded area shows $\pm 1\sigma$ uncertainties. Bottom: computation of the linear Pearson correlation coefficient of a fluorescence water model and the corresponding co-added residuals. Results from all dates can be found in Supplementary Figs. 7 and 8. The central wavenumber corresponds to the Doppler-corrected line centre of the seven most significant spectral H_2O lines.

(~1 km per pixel, from the Galileo regional mapping campaign), leading to limited information resulting from active geology.

Could the observed water vapour be linked to a subsurface ocean? At present, the most direct evidence that suggests a subsurface ocean exists on Europa was the detection of an induced magnetic field[28]. This field is likely to be produced in an electrically conductive near-surface region (for example, a global ocean of salty water). Moreover, geologic features have served as an indicator of the subsurface liquid water ocean[5]. Replication of Europa's terrain (ridges, pits, spots) suggests a thickness of the whole icy shell of a few kilometres up to 40 km, formed by an elastic lithosphere of <2 km and a ductile convecting layer from 4 to >20 km thick[5]. If one considers an ice layer ~5–20 km deep, we predict that an active vent would require an effective area with diameter of ~120–480 m to expel 2,095 tonnes of water vapour (see details in the subsection 'Estimates of vent properties' in Methods). These values should be taken as first-order estimates, given that we considered the ideal case scenario where the vent was described as a cylinder. In reality, we do not know the actual structure of Europan vent systems. Questions remain as to whether the observed activity might originate from intermediate liquid pockets closer to the surface, as well as to what mechanisms are responsible for the sporadic detections. Theoretical studies have indicated that, at low stresses and strains, ice will deform in an elastic (recoverable) manner. However, at relatively large strains, the ice would undergo irrecoverable deformation. At low temperatures this deformation will be accomplished by brittle failure, while at higher temperatures the result will be ductile creep[29]. Hence, the observed water vapour could issue from water pockets in the icy layer that act as pressurized chambers whose enclosed vapour escapes to space through narrow fissures, cracks, dikes, diapirs or a combination of all these. Decay of radioactive nuclei and tides[30] could increase heat and internal pressure in the subsurface environment to a point where short-lived break-ups occur, similar to water-driven mechanisms like the inferred pressure chambers on Enceladus[31]. Other possible source mechanisms for such water vapour activity include hydraulic flows[32], cryovolcanic eruptions[33] and/or vertical fracture channels along the icy sheet covering the subsurface ocean[27].

Theoretical approaches have provided valuable information about the Europan environment, yet observational astronomy has gathered limited details of exospheric water and other organics, including the expected temporal variability based on model predictions[19]. The results of our IR survey set global (upper) limits to the expected water vapour from exogenic sources and suggest that the tentative detection of water vapour resulted from a sporadic event, likely to be due to endogenic (plume-driven) activity. In fact, all individual detection strategies and wavelength regimes used to date have provided independent assessments that together convey the idea that observed features on Europa are transient and likely to be a result of plume activity (as suggested by the large number of non-detections in our survey and recent follow-up auroral observations with HST). However, these conclusions are strongly driven—and hampered—by the sensitivity limits of current ground and space-based facilities, making the detection of lower activity levels and proper characterization of Europa's atmosphere a complex endeavour with current technology. Considering these limitations, the research presented herein has developed our understanding of water vapour on Europa. Still, improved strategies from the ground should pursue follow-up observations in the 2.9-μm region with upgraded instrumentation featuring low noise detectors and higher sensitivity to spectral lines, as well as regularly scheduled time-serial searches for water rotational lines and organics with the Atacama Large Millimeter/submillimeter Array. In the mid-2020s, the 30-m-class telescopes (for example, the Thirty Meter Telescope and Extremely Large Telescope) will provide the sensitivity and angular resolution needed to better characterize Europa, overcoming current limitations of ~10-m-class ground-based facilities in the infrared.

From space, the access to fundamental bands of water and carbon dioxide with space assets such as the James Webb Space Telescope

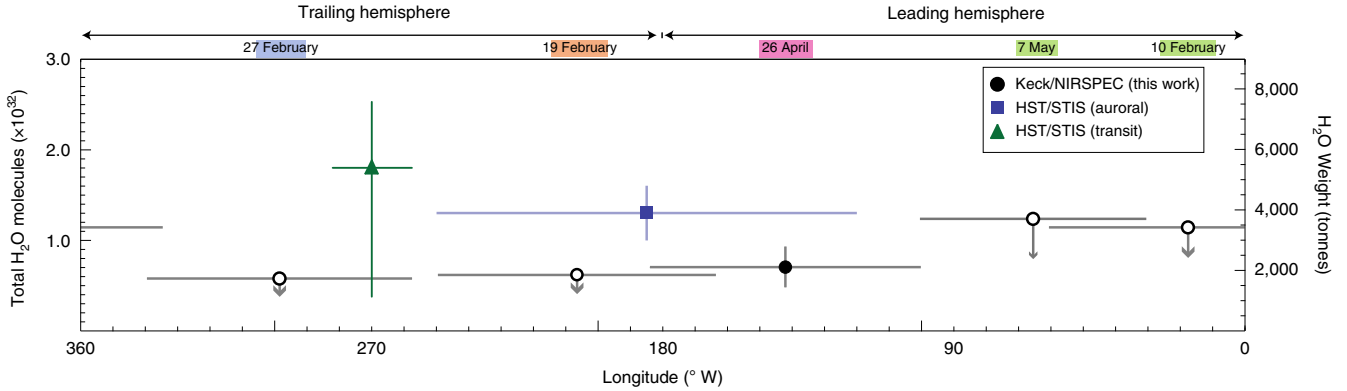

Fig. 2 | Most sensitive estimates of water versus longitudinal coverage. Global observations of water vapour can be put in perspective to previous localized estimates[15,16]. Our results show a rather quiescent state at most longitudes, with upper limits (unfilled black circles) of ~5.8×10^{31} H_2O molecules (minimum), ~8.8×10^{31} H_2O molecules (median). The tentative detection of water (filled black circle) on 26 April 2016 indicates plume content of $(7.0\pm2.2)\times10^{31}$ H_2O molecules (2,095 tonnes). Horizontal lines indicate longitudinal coverage (given by the field of view), while vertical lines represent $\pm1\sigma$ uncertainties. We show the median value resulting from the three measurements using transit observations[16] (green triangle) and the total range of $\pm1\sigma$ uncertainties (vertical line), as well as the auroral H and O results[15] (blue square). The sensitivity can be hampered by factors such as the sky conditions and (short) time on source. Supplementary Figs. 2 and 3 show an extended version with results from the complete survey.

(JWST) (expected to be operational in the early 2020s) might permit even more sensitive observations of water release at infrared wavelengths that could help to better understand the moon's activity and quiescent state. The JWST instruments (for example, NIRSpec integral field unit) will deliver spatial resolution on the order of 0.1″ (~340 km) at wavelengths near 3 μm that can yield better abundance constraints at low altitudes; in these regions, some hydrocarbons such as ethylene, methanol and hydrogen cyanide are expected to increase by an order of magnitude from night-to-day, while other species like methane, acetylene and ethane might show little relative change in column densities[19]. In ~2030, two major astronomical facilities, Europa Clipper and the JUpiter ICy moons Explorer (JUICE) mission, will provide giant leaps in our understanding of Europa and other Jovian moons. Featuring unparalleled sensitivity and spatial resolution, these in situ observations will obtain a closer assessment of active processes that shape the atmosphere. Ultimately, the study of fresh material released from potentially active vents promises to further unlock the secrets of Europa, especially tantalizing in light of the existence of subsurface aqueous environments on Europa and other ocean worlds in our Solar System.

Methods

Observing technique and strategy. Keck/NIRSPEC is a cross-dispersed echelle grating spectrometer, which features high sensitivity and high spectral resolving power. The cross-dispersed capability permits sampling of multiple spectral orders, facilitating the simultaneous detection of several molecules with high spectral resolving power (RP = $\lambda/\Delta\lambda\approx25{,}000$ with our slit configuration, where λ is wavelength), and allowing the measurement of individual line intensities. The high resolving power also reduces spectral confusion in crowded regions, while improving sensitivity by reducing background emission per resolution element.

Our observing strategy involved nodding the telescope in a four-step sequence 'ABBA' to cancel background emissions (where A and B represent relative positions of Europa 12″ apart along the instrument's slit). The data reduction and analysis of the acquired spectral frames included flat fielding, removal of pixels affected by high dark current and/or cosmic-ray hits, spatial and spectral rectification, and spatial registration of individual A and B beams. The technique and data analysis have been extensively discussed elsewhere[34–37]. This is a well-established technique that we have used effectively in the detection of water and organics in planetary atmospheres, exoplanets and small bodies. Therefore, we applied the same concepts from one sub-field to another sub-field in the search for water on Europa.

The analysis featured certain algorithms tailored to Europa's high-resolution spectral data. After combining the A and B beams from the (processed) difference frames, which further assists in removing any residual background emission, we extract spectra by summing 5 pixels (equal to ~1″, or 3,250 km) in the spatial direction and either 3 (0.4″ ≈ 1,500 km) or 5 pixels (0.7″ ≈ 2,500 km) for each row in the spectral direction depending on the slit width. This yields nearly disk-averaged measurements given Europa's diameter of ~1″. This strategy permitted us to cover about 10–20° in longitude per setting (time-dependent sub-observer W longitudes are shown in Table 2); however, the actual coverage was a factor of ~4 larger due to the slit width and its projection on Europa's disk. Supplementary Figs. 2 and 3 show the time-dependent longitude on the upper part of the figures, with a colour-coded identification on each date. The shaded red areas represent the actual slit coverage. Calibration of data was obtained through observations of flux standard stars with the 0.720″ × 24″ slit configuration. We used BS4471, BS5384, BS3982 in 2016; and BS3903, BS5685, BS4689 in 2017. For further details regarding flux calibration, please see the Supplementary Information.

In 2016, our strategy was to measure activity during Europa's orbit near the apocentre and pericentre to study the possible role of tidal effects on the presumed activity, but we also performed observations at other true anomalies (Supplementary Fig. 4). Weather conditions outside the dome were characterized by temperatures slightly above freezing. Image quality (seeing) was very good, as described by the observing characteristics in Table 1: seeing DIMM <1″, RH < 21%, wind speed < 22 mph, and low precipitable water vapour (PWV) < 1.5 mm in 2016. In 2017, we revisited some areas of interest based on the analysis of 2016 data, and also performed observations during eclipse and transit; however, the observing conditions in 2017 were somewhat hampered by higher humidity and PWV (up to 4.8 mm).

Data analysis. Despite the large distances between the Sun and the Jovian system, solar radiation is an efficient excitation mechanism at relatively large heliocentric distances—even beyond 6 AU (ref. [38])—allowing high-resolution spectroscopy to strategically sense water through non-resonance fluorescence at infrared wavelengths (so-called hot-band emission[39]). We targeted water lines (and organics) characterized by favourable transmission (Doppler shifted from their terrestrial counterparts) and low contamination from reflected solar absorption lines, which permitted sensitive measurements in the infrared.

We focused on two spectral regions: near ~2.9 μm and ~5.5 μm. The first region allowed us to measure (hot-band) water lines resulting from $(\nu_1+\nu_3)-\nu_1$, $(\nu_1+\nu_2+\nu_3)-(\nu_1+\nu_2)$, $2\nu_1-\nu_3$, and $(2\nu_1+\nu_3)-2\nu_1$ at ~2.9 μm, using NIRSPEC's KL1 and KL2 settings. The intrinsic characteristics of the KL1 setting allowed us to search for CH_3OH and C_2H_6, while the KL2 setting permitted searches for CH_4, NH_3, NH_2, HCN and H_2CO. In this Article, we report upper limits for CH_3OH and C_2H_6 relative to the tentative water detection on 26 April 2016, but defer the analysis on other dates to a future publication. The second region (at ~5.5 μm) allowed the characterization of water through the $\nu_3-\nu_2$, $\nu_1-\nu_2$ and $(\nu_2+\nu_3)-2\nu_2$ bands, using the M-wide setting; however, these observations had inferior sensitivity due to the changing sky conditions compared with those at ~2.9 μm, so we favoured results from observations at shorter wavelengths when available.

Analysis of Europa data accounted for intrinsic characteristics at the time of observations, such as heliocentric distance and orbital velocity of Europa (the Swings effect), geocentric distance and velocity (Doppler shift), and albedo (estimated). Once the spectra were calibrated, the core of our analysis was defined by a two-stage approach applied uniformly to the entire dataset, to minimize systematics and human error. Calibrated spectra contained information from molecular lines of Europa's atmosphere and continuum, and they can be characterized by at least four well-defined components: (1) Europa's continuum (reflected sunlight with Fraunhofer lines at the corresponding heliocentric velocity and geocentric velocity), (2) signatures from the terrestrial atmosphere, (3) instrument systematics and (4) possible Europan molecular lines (for instance, resulting from fluorescence emission).

The first stage of analysis employed the Levenberg–Marquardt least-squares fitting method to identify features 1–3, using synthetic modelling and noise analysis in the calibrated data. The fitting method is an iterative process until errors are minimized. To identify and isolate reflected solar features, we used a model for a disk-averaged solar spectrum that combines data from the spaceborne Atmospheric Chemistry Experiment (ACE)[40] and a purely theoretical model[41]. The Atmospheric Chemistry Experiment spectrum features very high resolving power ($R \approx 1 \times 10^5$ from 750–6,000 cm^{-1}); this model is then normalized to Europa's continuum in the combined spectrum (Supplementary Fig. 5 shows the continuum flux levels) and fitted with a transmittance function synthesized for the terrestrial atmosphere using the line-by-line radiative transfer model (LBLRTM[42]), which incorporates the HITRAN-2012 molecular database[43]. This standard data processing is able to retrieve the properties of the sky on each individual observing night (for example, the precipitable water vapour in Table 1), through synthetic modelling and fitting of the Earth's atmospheric conditions.

Removal of spectral fringing was performed on the residual spectra through Lomb-normalized periodogram analysis, from which we obtained the parameters (period, amplitude and phase) of the two strongest periodic features[44]. Next, we multiplied each synthetic periodic signal by the atmospheric transmittance and subtracted the product function from the residual spectra pixel by pixel. After fringe removal, noise analysis allowed us to identify systematics introduced by standard noise in our data, that is, errors resulting from unmodelled instrument harmonics and inaccuracies in terrestrial models. We developed different algorithms to reduce the standard noise by means of fast Fourier transform and wavelet analyses; however, we identified potential biasing of the data and opted for the leaner, and less invasive, approach of just removing the two strongest periodic features. Ultimately, our strategy sought to avoid any data processing that would alter or artificially enhance the spectra, and produce false positives.

In our methodology, the term residual refers to an observed spectrum whose components 1–3, described above, have been subtracted. In the second stage analysis, we used the residuals to retrieve abundances of Europan molecular species, using the Levenberg–Marquardt least-squares fitting method (mpfitfun function in Interactive Data Language, IDL), which fits a fluorescence water model[35] to the Europan spectrum (residuals) at a given rotational temperature. For a stronger statistical analysis, the mpfitfun fits all possible (water) lines from the residuals simultaneously. Through this methodology, mpfitfun yields the estimate of total molecules (and column density) from the measured flux (S) and a goodness-of-fit (F). The stochastic noise (N_{stoch}) is the photon noise of the spectrum (at each pixel), being typically largest at the position of sky emission lines. The 1σ uncertainty (or noise N) we use in our plots and calculations is a photon noise that is corrected by a factor F, so $N = N_{stoch}F$. In other words, the fitting algorithm characterizes noise with a factor F that indicates the amplitude of the actual noise component compared with the expected stochastic (photon-limited) noise. The statistics of noise estimates presented in this paper account for the larger error in our data (that is, the standard noise), thereby providing a more accurate estimate of SNRs. The SNR is the model signal (S) from the retrieval process, divided by the stochastic error (noise) times the goodness-of-fit (or, $SNR = S/[N_{stoch}F]$).

The fitting approach (in the second stage) allowed us to identify the spectral position of molecular lines (using our custom fluorescence models), and permitted the co-addition of the seven most significant spectral lines for each molecule[45]. In this context, the term significant spectral lines refers to lines with the highest fluorescence efficiency within the sampled wavelengths (for example, Supplementary Fig. 6 shows the seven most significant water lines from the 26 April 2016 data that were used to create the co-added spectrum in Fig. 1). Line co-adding used windows of ± 1 cm^{-1} from the Doppler-corrected line centre. Ultimately, this led to improvements in the SNR, and permitted both the evaluation of statistical significance of spectral lines in the residuals (at the expected position) and a comparison to the synthetic data using fluorescence models (for example, Fig. 1).

The final step in assessing a spectroscopic detection was to determine the significance level of the signal using a cross-correlation method between the residuals and the retrieved water model. For the cross-correlation, we used the IDL's correlate routine, which computed the linear Pearson correlation coefficient of the two vectors (that is, the integrated H_2O model spectrum of the seven most significative lines and the corresponding co-added NIRSPEC spectra), where the retrieved model serves as a robust filtering method to recognize the water fingerprint. The correlation values range from −1 to 1, with 1 indicating perfect correlation and 0 indicating no correlation between the two vectors. The co-added spectra and cross-correlation analysis of 2016 and 2017 data are shown in Supplementary Figs. 7 and 8, respectively. The correlation method of the 26 April data yielded a value of ~0.55 at the line centre.

Statistical analysis and the impact of noise. Potential false positives $<3\sigma$ can be seen throughout the parameter space at correlations <0.4, resulting from aliases generated by the correlation function of the model spectrum and the standard noise. To test the significance of our results, characterize noise, and understand its impact on the resulting analysis, we modelled 10^5 synthetic noise spectra and applied the same analytical strategies used on the analysis of Europan data. We created synthetic noise spectra following these steps: (1) calculate standard deviation from the NIRSPEC spectra (for example, using residuals on 26 April 2016), (2) create random noise using IDL's randomn function (with seeds from 1 to 10^5), and (3) multiply (random) noise by the standard deviation. From these simulations, we obtained the SNR and the corresponding correlations at the expected (water) line positions for each synthetic noise spectra. This methodology allowed us to test the analysis algorithm and prove if the noise calculation was accurate by fitting Gaussian curves to the resulting histograms (using the IDL's histogauss routine; Supplementary Fig. 9). The latter yielded the 1σ (68%), 2σ (95%) and 3σ (99.7%) confidence values from these noise simulations.

We obtained two key conclusions from this statistical analysis of simulated noise. First, we observed that the number of cases with $|SNR| \geq 3$ was 335, thus confirming a probability of 0.33% in 10^5 samples (that is, 3σ). Such estimate is in line with our calculation of SNR and validates the 3.1σ detection on 26 April 2016. And, second, the analysis indicated that the correlation level at 3σ was ~0.4, shown in correlation plots (green gradients in Fig. 1, Supplementary Figs. 7 and 8). Based on these findings, we observed that the number of cases with $|SNR| \geq 3$ and correlation ≥ 0.5 was 1 in 25,000 (or, 0.004% probability), making the tentative detection of water on Europa (26 April 2016) a statistically stronger case (3.9σ).

Based on these results, all of the following conditions were required to claim a tentative detection: (1) the least-squares fitting of Europa data and fluorescence model was consistent with a detection at $\geq 3\sigma$, (2) both co-added spectra of Europan lines and synthetic model match, and (3) correlation analysis of Europan spectra and synthetic model was larger than 0.4.

Calculation of column density and production rates. To measure column densities (molecules m^{-2}), we used a well-established formalism:

$$N_{col} = \frac{4\pi\Delta^2 F_{lines}}{gA_{FOV}} \quad (1)$$

where we identify spectral positions of each ro-vibrational transition within the sampled area (using least square fitting), allowing us to measure the fluxes at expected line positions, F_{lines} (W m^{-2}, at the top of the atmosphere corrected for telluric transmittance at the Doppler-shifted position of the line), the geocentric distance Δ (m), g is the fluorescence efficiency or g-factor (W $molecule^{-1}$) for individual molecular lines derived from our custom quantum mechanical fluorescence models at a given rotational temperature (for these calculations, we used three rotational temperatures (20 K, 50 K and 80 K) that are expected in expanding outgassing based on observations of expanding gases in analog—cometary—atmospheres), and A_{FOV} (m^2) is the area sampled by our field of view (3×5 pixels, or 5×5 pixels). Total molecules are obtained by multiplying N_{col} by A_{FOV}. Similarly, production rates (molecule s^{-1}) are obtained using the total molecules observed divided by the particle lifetime in the plume using the following formula:

$$Q = \frac{N_{col}A_{FOV}}{t} \quad (2)$$

where t is the particle lifetime in the plume. The lifetime is defined by a residence time of water particles in the plume of 887 s, as defined by ballistic trajectories: $t \approx 2\nu/g$, ν is particle speed of 583 m s^{-1}, using $\nu = \sqrt{3RT/M}$, where R is the ideal gas constant (8.314 kg m^2 s^{-2} mol K) and M is the molecular mass of water (0.018 kg mol^{-1}). Table 2 provides the resulting measurements of total water molecules resulting from our survey, and are displayed in Supplementary Figs. 7 and 8. Supplementary Table 1 shows the resulting water constraints at rotational temperatures of 20 K, 50 K and 80 K.

Estimates of vent properties. To first order, our tentative measurement of water vapour can provide an estimate of vent properties using a simple vent model with the following assumptions: (1) the gas behaves ideally, allowing us to define its behavior with the ideal gas law; (2) water vapour escapes from a reservoir to space through a vent with cylindrical shape; (3) the vent output consists of water vapour only. Using a range of possible plume temperatures (−10, 0 and 10 °C), we predict the plume vent would require an effective area of 0.01–0.18 km^2, or a diameter of ~120–480 m, to expel 7.0×10^{31} H_2O molecules (2,095 tonnes) through an ice layer ~5–20 km deep (see Supplementary Fig. 10). We note that the vent system could in reality be characterized by intricate networks of canals (as opposed to a perfect cylinder), but the modelling of these features is outside the scope of this paper. We describe the mathematical formalisms next. Our vent model uses the ideal gas law:

$$PV = nRT \quad (3)$$

where P is pressure (atm), V is volume (m^3), R is 8.2×10^{-5} m^3 atm K^{-1} mol^{-1}, T is temperature (K) and n is number of moles of gas (mol). We define:

$$n = Q_T/A \quad (4)$$

where Q_T is the total molecules (7×10^{31} molecules), and A is Avogadro's constant ($6.022140857 \times 10^{23}$ molecules mol^{-1}). We define the vent chamber as a cylinder, whose volume V (m^3) = area (m^2) × length (m), with area = π × radius^2. Therefore, the vent's area can be defined as:

$$\text{Area} = \frac{nRT}{P \times \text{length}} \quad (5)$$

with units: area (m^2), n (mol), R (m^3 atm K^{-1} mol^{-1}), T (K), P (atm) and length (m). There are special correlation equations for the gas–liquid saturation properties

of water, and we used the internationally accepted formulation for the properties of light and heavy steam water using equation (1) in (ref. [46]), which defines the thermodynamic properties of ordinary water at saturation:

$$P = \rho_c \exp\left(a_1\tau + a_2^{1.5} + a_3^3 + a_4^{3.5} + a_5^4 + a_6^{7.5}\right) T_c/T$$

with $\tau = 1 - T/T_c$, $T_c = 647.096$ K, $\rho_c = 22{,}064$ kPa, $a_1 = -7.85951753$, $a_2 = 1.84408259$, $a_3 = -11.7866497$, $a_4 = 22.6807411$, $a_5 = -15.9618719$ and $a_6 = 1.80122502$.

To convert units of atm to kPa, we used the relation: $P_{kPA} = P_{atm}/101.325$. T (K) is the independent temperature variable, for which in this exercise we employed −10, 0 and 10 °C.

Data availability

All data are publicly available at the Keck Observatory Archive. Any other details of this work are available from the corresponding author on reasonable request.

Received: 25 January 2019; Accepted: 30 September 2019;
Published online: 18 November 2019

References

1. Greeley, R. et al. Europa: initial Galileo geological observations. *Icarus* **135**, 4–24 (1998).
2. Greenberg, R., Hoppa, G. V., Tuffs, B. R., Geissler, P. E. & Reilly, J. Chaos on Europa. *Icarus* **141**, 263–286 (1999).
3. Anderson, J. D. et al. Europa's differentiated internal structure: inferences from four Galileo encounters. *Science* **281**, 2019–2022 (1998).
4. Carr, M. H. et al. Evidence for a subsurface ocean on Europa. *Nature* **391**, 363–365 (1998).
5. Pappalardo, R. T. et al. Does Europa have a subsurface ocean? Evaluation of the geological evidence. *J. Geophys. Res.* **104**, 5–24 (1999).
6. Schubert, G., Anderson, J. D., Spohn, T. & McKinnon, W. B. in *Jupiter: The Planet, Satellites and Magnetosphere* (eds Bagenal, F., Dowling, T. E. & McKinnon, W. B. 281–306 (Cambridge Univ. Press, 2004).
7. Johnson, R. E. & Sundqvist, B. U. R. Sputtering and detection of large organic molecules from Europa. *Icarus* **309**, 338–344 (2018).
8. Johnson, R. E., Killen, R. M., Waite, J. H. & Lewis, W. S. Europa's surface composition and sputter-produced atmosphere. *Geophys. Res. Lett.* **25**, 3257–3260 (1998).
9. Brown, M. E. Potassium in Europa's atmosphere. *Icarus* **151**, 190–195 (2001).
10. Mauk, B. H. et al. Energetic ion characteristics and neutral gas interactions in Jupiter's magnetosphere. *J. Geophys. Res.* **109**, A09S12 (2003).
11. Shematovich, V. I., Johnson, R. E., Cooper, J. F. & Wong, M. C. Surface-bounded atmosphere of Europa. *Icarus* **173**, 480–498 (2005).
12. Cassidy, T. A. et al. Magnetospheric ion sputtering and water ice grain size at Europa. *Planet. Space Sci.* **77**, 64–73 (2013).
13. Vorburger, A. & Wurz, P. Europa's ice-related atmosphere: the sputter contribution. *Icarus* **311**, 135–145 (2018).
14. Nimmo, F., Pappalardo, R. T. & Cuzzi, J. Observational and theoretical constraints on plume activity at Europa. In *AGU Fall Meeting 2007* P51E-05 (AGU, 2007).
15. Roth, L. et al. Transient water vapor at Europa's South Pole. *Science* **343**, 171–174 (2014).
16. Sparks, W. B. et al. Probing for evidence of plumes on Europa with HST/STIS. *Astrophys. J.* **829**, 121 (2016).
17. Jia, X., Kivelson, M. G., Khurana, K. K. & Kurth, W. S. Evidence of a plume on Europa from Galileo magnetic and plasma wave signatures. *Nat. Astron* **2**, 459–464 (2018).
18. Arnold, H., Liuzzo, L. & Simon, S. Magnetic signatures of a plume at Europa during the Galileo E26 flyby. *Geophys. Res. Lett.* **46**, 1149–1157 (2019).
19. Teolis, B. D., Wyrick, D. Y., Bouquet, A., Magee, B. A. & Waite, J. H. Plume and surface feature structure and compositional effects on Europa's global exosphere: preliminary Europa mission predictions. *Icarus* **284**, 18–29 (2017).
20. Smyth, W. H. & Marconi, M. L. Europa's atmosphere, gas tori, and magnetospheric implications. *Icarus* **181**, 510–526 (2006).
21. Plainaki, C. et al. The role of sputtering and radiolysis in the generation of Europa exosphere. *Icarus* **218**, 956–966 (2012).
22. Tiscareno, M. S. & Geissler, P. E. Can redistribution of material by sputtering explain the hemispheric dichotomy of Europa? *Icarus* **161**, 90–101 (2003).
23. Cassidy, T. A., Johnson, R. E. & Tucker, O. J. Trace constituents of Europa's atmosphere. *Icarus* **201**, 182–190 (2009).
24. Huybrighs, H. L. et al. On the in-situ detectability of Europa's water vapour plumes from a flyby mission. *Icarus* **289**, 270–280 (2017).
25. Hurford, T. A., Helfenstein, P., Hoppa, G. V., Greenberg, R. & Bills, B. G. Eruptions arising from tidally controlled periodic openings of rifts on Enceladus. *Nature* **447**, 292–294 (2007).
26. Hedman, M. M. et al. An observed correlation between plume activity and tidal stresses on Enceladus. *Nature* **500**, 182–184 (2013).
27. Rhoden, A. R., Hurford, T. A., Lorenz, R. & Retherford, K. Linking Europa's plume activity to tides, tectonics, and liquid water. *Icarus* **253**, 169–178 (2015).
28. Kivelson, M. G. et al. Galileo magnetometer measurements: a stronger case for a subsurface ocean at Europa. *Science* **289**, 1340–1343 (2000).
29. Nimmo, F. & Manga, M. in *Europa* (ed. Pappalardo, R. T. et al.) 381–404 (Univ. of Arizona Press, 2009).
30. Moore, W. B. & Hussmann, H. Thermal evolution of Europa's silicate interior. In *Europa* (ed. Pappalardo, R. T. et al.) 369–380 (Univ. of Arizona Press, 2009).
31. Johnston, S. A. & Montési, L. G. J. Formation of ridges on Europa above crystallizing water bodies inside the ice shell. *Icarus* **237**, 190–201 (2014).
32. Schmidt, B. E., Blankenship, D. D., Patterson, G. W. & Schenk, P. M. Active formation of 'chaos terrain' over shallow subsurface water on Europa. *Nature* **479**, 502–505 (2011).
33. Quick, L. C., Barnouin, O. S., Prockter, L. M. & Patterson, G. W. Constraints on the detection of cryovolcanic plumes on Europa. *Planet. Space Sci.* **86**, 1–9 (2013).
34. Bonev, B. P. *Towards a Chemical Taxonomy of Comets: Infrared Spectroscopic Methods for Quantitative Measurements of Cometary Water (with an Independent Chapter on Mars Polar Science*. PhD thesis, Univ. Toledo (2005).
35. Villanueva, G. L. et al. Water in planetary and cometary atmospheres: H_2O/HDO transmittance and fluorescence models. *J. Quant. Spectrosc. Radiat. Transf.* **113**, 202–220 (2012).
36. Paganini, L. et al. The formation heritage of Jupiter-family comet 10P/Tempel 2 as revealed by infrared spectroscopy. *Icarus* **218**, 644–653 (2012).
37. Villanueva, G. L. et al. Strong water isotopic anomalies in the Martian atmosphere: probing current and ancient reservoirs. *Science* **348**, 218–221 (2015).
38. Paganini, L. et al. Ground-based infrared detections of CO in the Centaur-Comet 29P/Schwassmann–Wachmann 1 at 6.26 AU from the Sun. *Astrophys. J.* **766**, 100 (2013).
39. Mumma, M. J. et al. Detection of abundant ethane and methane, along with carbon monoxide and water, in comet C/1996 B2 Hyakutake: evidence for interstellar origin. *Science* **272**, 1310–1314 (1996).
40. Hase, F. et al. An empirical line-by-line model for the infrared solar transmittance spectrum from 700 to 5000 cm^{-1}. *J. Quant. Spectrosc. Radiat. Transf.* **102**, 450–463 (2006).
41. Kurucz, R. L. The solar irradiance by computation. http://kurucz.harvard.edu/sun.html (Harvard, 1997).
42. Clough, S. A. et al. Atmospheric radiative transfer modeling: a summary of the AER codes. *J. Quant. Spectrosc. Radiat. Transf.* **91**, 233–244 (2005).
43. Rothman, L. S. et al. The HITRAN2012 molecular spectroscopic database. *J. Quant. Spectrosc. Radiat. Transf.* **130**, 4–50 (2013).
44. Villanueva, G. L. et al. A sensitive search for organics (CH_4, CH_3OH, H_2CO, C_2H_6, C_2H_2, C_2H4), hydroperoxyl (HO_2), nitrogen compounds (N_2O, NH_3, HCN) and chlorine species (HCl, CH_3Cl) on Mars using ground-based high-resolution infrared spectroscopy. *Icarus* **223**, 11–27 (2013).
45. Paganini, L., Mumma, M. J., Gibb, E. L. & Villanueva, G. L. Ground-based detection of deuterated water in comet C/2014 Q2 (Lovejoy) at IR wavelengths. *Astrophys. J. Lett.* **836**, L25–L31 (2017).
46. Wagner, W. & Pruss, A. International equations for the saturation properties of ordinary water substance. Revised according to the international temperature scale of 1990. Addendum to *J. Phys. Chem. Ref. Data* **16**, 893 (1987). *J. Phys. Chem. Ref. Data* **22**, 783–787 (1993).

Acknowledgements

We thank the staff of the W. M. Keck Observatory for their support throughout our long Europa observation programme. L.P. acknowledges support from NASA's Keck PI Awards (grant numbers RSA 1541943, 1466335), Solar System Observations (grant number NNX17AI85G) and Solar System Workings (grant number 80NSSC19K0811). L.R. is supported by the Swedish Research Council (2017-04897). The authors recognize and acknowledge the very important cultural role and reverence that the summit of Maunakea has always had within the indigenous Hawaiian community. We are most fortunate to have the opportunity to conduct observations from this mountain.

Author contributions

L.P. and L.R. planned and performed the astronomical observations and strategy. L.P., G.L.V., A.M.M. and T.A.H. contributed to data analysis. All authors contributed to the interpretation of results.

Competing interests

The authors declare no competing interests.

Additional information

Supplementary information is available for this paper at https://doi.org/10.1038/s41550-019-0933-6.

Correspondence and requests for materials should be addressed to L.P.

Peer review information *Nature Astronomy* thanks Melissa McGrath and the other, anonymous, reviewer(s) for their contribution to the peer review of this work.

Reprints and permissions information is available at www.nature.com/reprints.

Publisher's note Springer Nature remains neutral with regard to jurisdictional claims in published maps and institutional affiliations.